


Evidence of distinct nonpolar/polar ordering at long/short ranges in relaxor ferroelectrics

Anuvrat Tripathi¹,¹ Sanjit Ghose,² Rudolph Erasmus³,³ and Saurabh Tripathi^{1,*}¹Department of Physics, Indian Institute of Technology (BHU), Varanasi 221005, India²National Synchrotron Light Source II, Brookhaven National Laboratory, Upton, New York 11973, USA³Materials for Energy Research Group, Material Physics Research Institute, School of Physics, University of the Witwatersrand, Johannesburg 2000, South Africa (Received 24 September 2024; revised 9 November 2024; accepted 18 December 2024; published 9 January 2025)

Distinct atomic nonpolar/polar ordering is determined at long, intermediate, and short ranges using synchrotron x-ray diffraction, Raman scattering, and pair distribution function data in $K_{0.5}Na_{0.5}NbO_3$ -doped $BaTiO_3$ -based relaxor ferroelectrics, viz., $(1-x)Ba_{0.9}Sr_{0.1}TiO_3-xKNN50$. Two different polar phases with distinct symmetries are identified at short/intermediate ranges for $x = 0.10$, where a monoclinic phase at short ranges gradually transforms into a rhombohedral phase at intermediate ranges. In contrast, a nonpolar phase with average cubic symmetry is found to be stable at long ranges for a wide temperature range ($100 \leq T \leq 500$ K). The polar behavior of short/intermediate-range ordering is quantified in terms of the amplitude of ferroelectric phonon mode Γ_4^- ($q = 0, 0, 0$) (which corresponds to the zone center of the cubic Brillouin zone). The amplitude of the Γ_4^- phonon mode increases with decreasing temperature, suggesting the enhancement of ferroelectric polarization at short/intermediate ranges on lowering temperatures. Enhanced ferroelectric polarization at low temperature is also visible and evident by ferroelectrostriction and is quantified by the increase in magnitude of spontaneous volume ferroelectrostriction. Consequently, Zero thermal expansion is observed at low temperatures.

DOI: [10.1103/PhysRevB.111.024104](https://doi.org/10.1103/PhysRevB.111.024104)

I. INTRODUCTION

Various properties of perovskite-based smart materials can be tailored by engineering atomic ordering at various length scales. Among perovskite-based smart materials, relaxor ferroelectrics (or relaxors) have been widely studied for their numerous applications, including electrical energy storage systems, sensors and actuators, medical ultrasonic imaging, and many more [1,2]. The relaxors possess distinct structures at long and short ranges that are responsible for various fascinating properties. Unlike ordered systems, relaxor ferroelectrics such as $PbMg_{1/3}Nb_{2/3}O_3$ (PMN) [3], $PbSc_{1/2}Ta_{1/2}O_3$ [4], $PbZn_{1/3}Nb_{2/3}O_3$ (PZN) [5], etc., exhibit chemical heterogeneity that leads to disorder, resulting in enhanced physical responses [1,2]. The relaxor behavior is often linked to the presence of polar nanoregions (PNRs), which nucleate and start growing below the Burns temperature T_B [1,6,7]. The presence of PNRs and their interactions are considered to be responsible for various physical properties observed in relaxor materials [1,8].

Among various intriguing properties exhibited by perovskite-based oxides, controlled thermal expansion/negative thermal expansion (NTE) is scientifically and technologically important [9–12]. NTE/zero thermal expansion (ZTE) in perovskite-based ferroelectrics is attributed to ferroelectrostriction, which is driven by large ferroelectric displacements resulting from the strong covalent

nature of the A/B -O bonds [13–18]. Ferroelectrostriction in perovskite-based relaxor ferroelectrics arises from the enhanced correlations among intra/interpolar clusters (PNRs) exhibiting ferroelectric (or polar) distortions [8,19]. The ferroelectric (or polar) distortions responsible for ferroelectrostriction are associated with the freezing of a soft phonon mode corresponding to the zone center of the cubic Brillouin zone ($q = 0, 0, 0$) [20–22]. Among various phonon modes corresponding to the Γ point of the cubic Brillouin zone, a triply degenerate Γ_4^- phonon mode (often known as the ferroelectric mode) is responsible for ferroelectric (or polar) ordering. The freezing of the Γ_4^- phonon mode along various dimensions leads to various low-symmetry phases of $BaTiO_3$, viz., $P4mm$, $Amm2$, and $R3m$ with $(a, 0, 0)$, $(a, a, 0)$, and (a, a, a) order parameter directions (OPDs), respectively. Hence, the frozen phonon mode approach (symmetry mode analysis) can be used to quantify the ferroelectric (polar) distortions. [20–22]. Most prominent relaxor ferroelectrics are Pb based, viz., PZN [9], PMN [12], etc. Due to the harmful effects of Pb on the environment and humans, various alternatives, viz., $Ba(Zr,Ti)O_3$ [23], $Ba(Sn,Ti)O_3$ [24], $(K,Na)NbO_3$ [25], $(K,Na,Ba,Sr)(Nb,Ti)O_3$ [26–28], and other related materials, have been widely studied.

The alkali niobate-based system, i.e., $K_{0.5}Na_{0.5}NbO_3$ (KNN50), has been widely studied because of its enhanced physical responses, which are due to the presence of morphotropic phase boundary [21,25,29–32]. Orayech *et al.* reported a series of structural phase transitions, viz., $R3c \xrightarrow{\approx 135 \text{ K}} Amm2 \xrightarrow{\approx 465 \text{ K}} P4mm \xrightarrow{\approx 700 \text{ K}} Pm\bar{3}m$ as a function of temperature using x-ray and neutron diffraction

*Contact author: stripathi.phy@itbhu.ac.in

data [21]. Moreover, later Kong *et al.* reported another series of phase transitions, viz., $Pm \xrightarrow{\approx 471 \text{ K}} P4mm \xrightarrow{\approx 674 \text{ K}} Pm\bar{3}m$, where a monoclinic phase is found to be stable down to the lowest studied temperature [25]. Further, Gupta *et al.* and Kong *et al.* confirmed the monoclinic symmetry at short ranges using pair distribution function (PDF) data [25,33].

Moreover, the alkaline earth metal based perovskite BaTiO_3 and its solid solutions have also been widely studied as a potential alternative to Pb-based materials. The doping of elements like strontium at the *A* site induces disorder/relaxor behavior in the material. Among various compositions of Sr-doped BaTiO_3 , i.e., $\text{Ba}_{(1-x)}\text{Sr}_x\text{TiO}_3$, the maximum dielectric response at ambient conditions is observed for $x = 0.10$ (BST10). BST10 undergoes structural phase transitions similar to those of BaTiO_3 , i.e., $R3m \rightarrow Amm2 \rightarrow P4mm \rightarrow Pm\bar{3}m$, but with a shift in T_C ($\approx 369 \text{ K}$) to lower temperatures [34–38]. Among other Pb-free alternatives, KNN50-doped BaTiO_3 (KBT x) has been studied for its unique structural properties at short and long ranges, leading to the discovery of the morphotropic relaxor boundary [28]. Moreover, some authors have doped Sr at the *A* site of KBT x to enhance the disorder/relaxor property of the ceramics [26,27].

In the present work, we chose Pb-free Sr-doped BaTiO_3 , i.e., $\text{Ba}_{0.9}\text{Sr}_{0.1}\text{TiO}_3$ (BST10), as one of the parents due to its maximum dielectric response [34–37] and KNN50 as the other parent to form a solid solution, viz., $(1-x)\text{BST10}-x\text{KNN50}$ (BKST x). The crystal structures at long ranges, along with various electrical properties, are determined for BKST x ($x = 0, 0.05, 0.10$) ceramics. A relaxor behavior is observed for $x = 0.10$ (BKST10) in temperature-dependent dielectric data. Moreover, the atomic ordering at various length scales (long, intermediate, and short) for BKST10 is determined using temperature-dependent synchrotron x-ray diffraction, Raman scattering, and pair distribution function data. The ferroelectric displacements at various length scales are quantified by calculating the amplitude of structural distortion modes using ISODISTORT. In addition, spontaneous volume ferroelectrostriction (SVFS) is calculated using the Debye-Grüniesen equation.

II. EXPERIMENTAL PROCEDURE

The BKST x ($x = 0.00, 0.05, \text{ and } 0.10$) ceramics were prepared using a solid-state reaction technique. The precursors, viz., K_2CO_3 (Sisco Research Laboratories; 99%), Na_2CO_3 (HIMIDEA Labs; 99.5%), BaCO_3 (HIMIDEA Labs; 99%), SrCO_3 (HIMIDEA Labs; 99%), Nb_2O_5 (HIMIDEA Labs; 99.9%), and TiO_2 (HIMIDEA Labs; 99%), were preheated in an oven at 393 K. The heated powders were weighed per stoichiometry and mixed via milling for 24 h. After milling, the powder slurry was dried and calcined at 1173–1223 K for 4 h. The pellets were formed at 8–10 metric tons of pressure and sintered at 1423–1473 K for 3 h. The room temperature x-ray diffraction data were collected over the 2θ range 20° – 120° with a step size of 0.02 from a Rigaku Miniflex 600 x-ray diffractometer with Cu $K\alpha$ radiation. The sintered pellets were electroded with silver paste on both sides for the dielectric and Polarisation vs. Electric field (PE) loop measurements. The dielectric measurements were carried out

using a Keysight LCR meter with a frequency and temperature range of 1 kHz to 1 MHz and $100 \leq T \leq 650 \text{ K}$, respectively. For PE loop measurements at 10 Hz frequency, Radiant Technology's Precision LCII Ferroelectric Tester was used. The temperature-dependent synchrotron x-ray diffraction measurements were performed at the 28-ID-2 (XPD) beamline at the National Synchrotron Light Source II at Brookhaven National Laboratory with $\lambda = 0.1821 \text{ \AA}$ for a temperature range of $100 \leq T \leq 500 \text{ K}$. The intermediate- and short-range crystal structure was analyzed using temperature-dependent Raman scattering and PDF data. The temperature-dependent Raman spectra were obtained with a Horiba LabRAM HR Raman spectrometer with an Olympus BX41 microscope attachment with an excitation wavelength of 514.5 nm from a Lexel Model-95 argon ion laser. The samples were placed in a Linkam THMS600 microscope stage for Raman measurements at varying temperatures. A $50\times$ Long Working Distance (LWD) objective lens (numerical aperture = 0.50) was used to focus the laser beam onto the samples, and the backscattered light was dispersed using a 600 lines/mm grating onto a liquid-nitrogen-cooled CCD detector. Data acquisition was carried out with LABSPEC version 5 software. The laser power at the sample was approximately 0.4 mW, which was confirmed to ensure there were no local heating effects from the laser. The spectral range for this study was selected to span from 80 to 1900 cm^{-1} .

The PDF data were obtained from the high-energy synchrotron x-ray diffraction (SXRD) data, which were reduced to the total scattering structure function $S(Q)$, given as [39,40]

$$S(Q) = 1 + \frac{[I^{\text{coh}}(Q) - \sum c_i |f_i(Q)|^2]}{|\sum f_i(Q) c_i|^2}, \quad (1)$$

where Q is defined as $Q = 4\pi \sin\theta/\lambda$ and is referred to as the wave vector, 2θ is the angle between incident and diffracted beams, I^{coh} corresponds to the coherent part of the diffraction data, and c_i and $f_i(Q)$ are the atomic concentrations and x-ray structure factor of atomic species of the i th type. $S(Q)$ was then transformed to the final pair distribution function $G(r)$ via Fourier transformation with $Q_{\text{max}} = 23.6 \text{ \AA}^{-1}$ [39,40]:

$$G(r) = \frac{2}{\pi} \int_{Q_{\text{min}}}^{Q_{\text{max}}} Q[S(Q) - 1] \sin(Qr) dQ, \quad (2)$$

where $Q_{\text{min}} = 0.65 \text{ \AA}^{-1}$.

Further, the decomposition of phonon modes was done using the ISODISTORT tool available online [41,42].

III. RESULTS AND DISCUSSION

A. XRD analysis of BKST x ceramics

The structural analysis of BKST x ($x = 0.00, 0.05, \text{ and } 0.10$) ceramics is given in the Supplemental Material [43]. The parent, i.e., $x = 0.00$ (BKST0), exhibits tetragonal symmetry (space group: $P4mm$ [$a_0^0 a_0^0 c_0^+$]), which transforms to cubic (space group: $Pm\bar{3}m$ [$a_0^0 a_0^0 a_0^0$]) for both $x = 0.05$ (BKST5) and 0.10 (BKST10; see Figs. 1 and 2 in the Supplemental Material [43]). The electrical properties of BKST x ceramics are discussed in the next section.

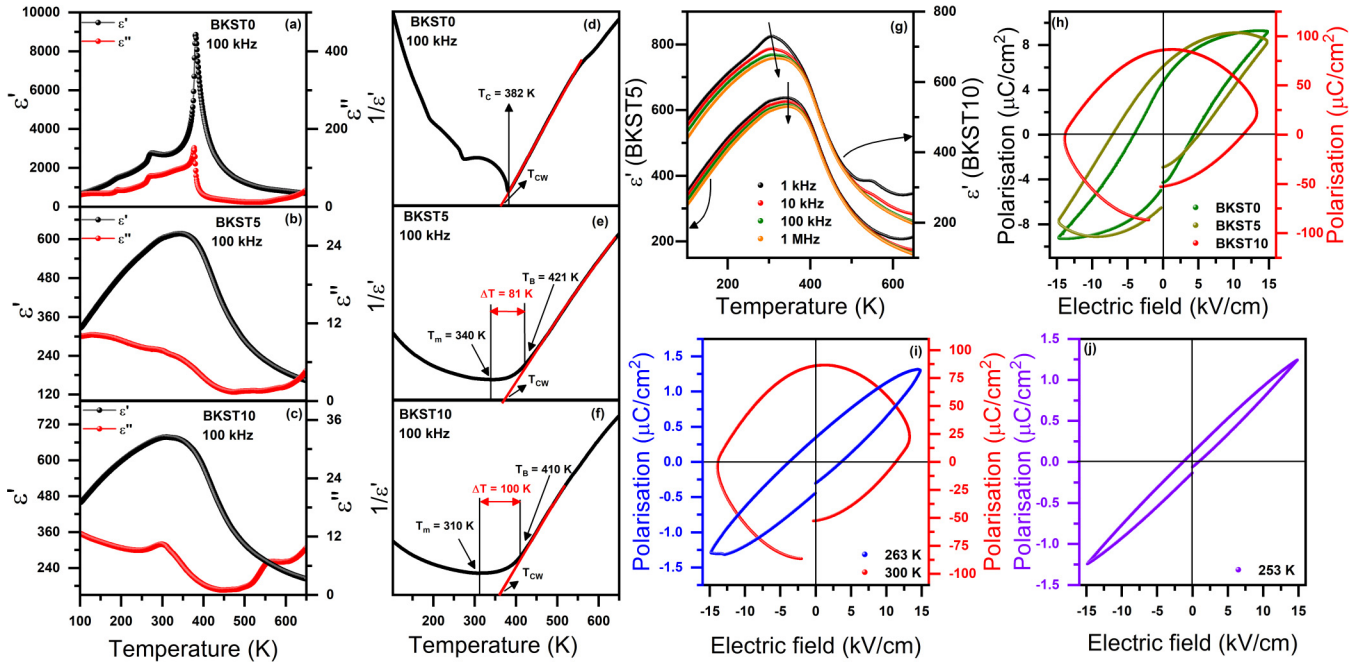


FIG. 1. Electrical properties of BKST x ceramics, including (a)–(c) the temperature-dependent real (ϵ') and imaginary (ϵ'') parts of BKST x ceramics, (d)–(f) a plot of the inverse of the real part of the dielectric constant with temperature, i.e., $1/\epsilon'$ vs T for BKST0, BKST5, and BKST10 ceramics at 100 kHz, (g) a frequency-dependent plot of the real part of the dielectric constant ϵ' vs temperature for BKST5 and BKST10 ceramics, (h) PE loops for BKST x ceramics, and (i) and (j) the temperature-dependent evolution of the PE loop for BKST10 ceramics at 253, 263, and 300 K.

B. Dielectric and PE loops of BKST x ceramics

The temperature-dependent dielectric measurements for all the compositions were carried out for a wide temperature range ($100 \leq T \leq 650$ K). Figures 1(a)–1(c) show the temperature-dependent dielectric behavior [real (ϵ') and imaginary (ϵ'') parts] for BKST0, BKST5, and BKST10 ceramics at 100 kHz. For BKST0, three dielectric peaks are observed, which are attributed to the three phase transitions, viz., $Pm\bar{3}m \xrightarrow{\approx 382 \text{ K}} P4mm \xrightarrow{\approx 274 \text{ K}} Amm2 \xrightarrow{\approx 192 \text{ K}} R3m$, similar to those of $BaTiO_3$ with a decrease in T_C [44,45]. A single broad and diffuse dielectric peak is observed with increasing KNN50 content, i.e., for BKST5 and BKST10 ceramics, suggesting the presence of a diffuse phase transition. Additionally, T_m shifts towards room temperature with increasing KNN50 content [see Figs. 1(d)–1(f)]. The normal ferroelectrics follow the Curie-Weiss law above Curie temperature, while the dielectric behavior of disordered ferroelectrics (exhibiting a diffused dielectric peak) deviates away from the Curie-Weiss law below a certain temperature referred to as the Burns temperature T_B [1,26,46]. The nucleation and growth of PNRs begins below the Burns temperature [1,2,8]. The diffuseness of the dielectric peak can be analyzed and quantified by calculating the deviation from the Curie-Weiss law ΔT_m , which is given as [26,47]

$$\Delta T_m = T_B - T_m, \quad (3)$$

where T_B denotes the Burns temperature and T_m is the temperature corresponding to the dielectric maximum. Figures 1(d)–1(f) show plots of the inverse of the real part of the dielectric

permittivity vs temperature ($1/\epsilon'$ vs T) and depict the diffuseness ΔT_m of the dielectric peaks with increasing KNN50 content. For BKST0 the dielectric behavior follows the Curie-Weiss law. On the other hand, for BKST5, $\Delta T_m = 81$ K, while for BKST10, $\Delta T_m = 100$ K, which implies an increase in the diffuseness of the dielectric peak and hence the disorder in the system with increasing KNN50 content [26], which is further supplemented by PE loops.

Figure 1(h) represents the PE loops of BKST x ceramics. For BKST0, the loop dictates ferroelectric behavior similar to that of $BaTiO_3$ [48], while the shape of the loop changes with increasing KNN50 content. Ferroelectric (FE) loops for BKST5 and BKST10 ceramics depict increasing disorder in the system, finally demonstrating a linear lossy dielectric behavior for BKST10 ceramics [49]. Hence, the maximum disorder is observed for BKST10 ceramics, which is further analyzed for its relaxor behavior. Figure 1(g) depicts the frequency-dependent behavior of the real part of the dielectric constant as a function of temperature. A frequency dispersion of $\Delta T \approx 6$ K is observed in BKST10 ceramics, while BKST5 ceramics do not exhibit any frequency dispersion [see Fig. 1(g)]. This suggests that BKST10 is a potential relaxor, while BKST5 exhibits only a diffuse phase transition. Moreover, Figs. 1(i) and 1(j) depict the temperature-dependent PE loops for BKST10. It is clearly evident from Figs. 1(i) and 1(j) that the shape of the loop changes with decreasing temperature, dictating the transformation of a linear lossy dielectric to a relaxorlike behavior, suggesting enhancement in cationic ordering [19,49].

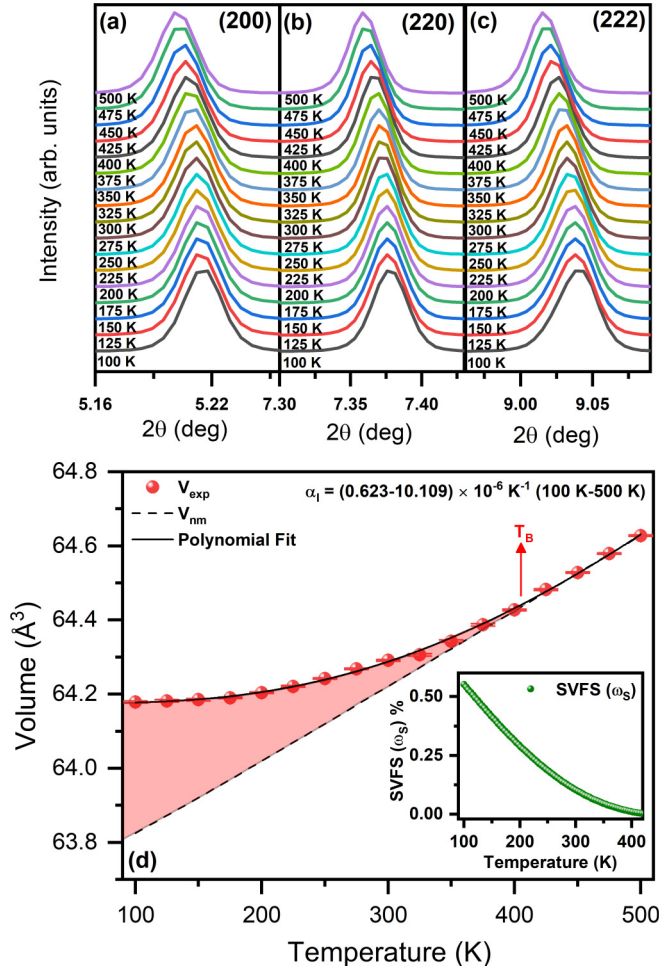


FIG. 2. (a)–(c) Temperature-dependent evolution of the main perovskite peaks, viz., (200), (220), and (222), of BKST10 ceramics for the wide range of temperature ($100 \leq T \leq 500$ K), respectively. (d) Temperature-dependent evolution of the volume for BKST10 ceramics. The symbols represent the experimental volume; solid and dashed lines represent the polynomial fit of the experimental volume and nominal volume V_{nm} , respectively. The inset shows the temperature-dependent evolution of spontaneous volume ferroelectricity calculated using interpolated volume data.

C. SXR analysis and zero thermal expansion in BKST10 ceramics

Owing to the relaxor behavior observed for BKST10 ceramics, the temperature-dependent evolution of the long-range crystal structure of BKST10 is analyzed. Figures 2(a)–2(c) depict the evolution of the main perovskite peaks, viz., (200), (220), and (222), observed in the SXR pattern of BKST10 ceramics for a wide temperature range ($100 \leq T \leq 500$ K). The peaks do not split and exhibit a singlet nature throughout the temperature range, which suggests the presence of cubic symmetry down to the lowest studied temperature. The cubic symmetry (space group: $Pm\bar{3}m$) is confirmed by analyzing the SXR data using the Rietveld refinement program available in the FULLPROF suite [50]. Moreover, Fig. 2(d) depicts the volume as a function of temperature for BKST10 ceramics. The volume deviates from the linear behavior below the Burns temperature ($T_B \approx 410$ K),

which is determined using the inverse of temperature-dependent dielectric data [see Fig. 1(f)]. The volume begins to saturate at low temperatures, indicating zero thermal expansion in the material.

The nearly temperature-independent volume observed at low temperatures for BKST10 ceramics suggests ZTE in the material [see Fig. 2(d)]. The ZTE is quantified using the volumetric coefficient of thermal expansion α_V , which is defined as follows [13]:

$$\alpha_V = \frac{1}{V} \frac{\partial V}{\partial T}, \quad (4)$$

where V corresponds to volume at temperature T [13,51]. For cubic systems, the volumetric thermal expansion coefficient α_V is 3 times the linear thermal expansion coefficient α_l , i.e., $\alpha_V = 3\alpha_l$ [13]. For BKST10 ceramics, the calculated linear thermal expansion coefficient α_l ranges between 0.623 and $10.109 \times 10^{-6} \text{ K}^{-1}$ (100–500 K), which suggests ZTE behavior in BKST10 ceramics [19].

As discussed earlier, the NTE/ZTE in perovskite-based materials results from ferroelectrostriction. The ferroelectrostriction causes volume gain (or the ferroelectrovolume effect) [12] in the material, which can be quantified using SVFS, which is defined as [13,14,16]

$$\omega_S = \frac{V_{exp} - V_{nm}}{V_{nm}} \times 100\%, \quad (5)$$

where ω_S represents SVFS and V_{exp} and V_{nm} correspond to experimental and nominal volumes, respectively. V_{exp} is obtained from the lattice parameter after refinement, while V_{nm} is obtained after fitting the experimental volume using the Debye-Grüniesen equation in the temperature range of $400 \leq T \leq 500$ K (see the Supplemental Material [43]) as the deviations begin near the Burns temperature ($T_B \approx 410$ K) [13,51,52].

Figure 2(d) depicts the ZTE behavior of BKST10 ceramics. The volume gain arising from the ferroelectrostriction can be clearly observed. The inset depicts the evolution of SVFS ω_S with temperature. The SVFS (or ferroelectrostriction) increases with decreasing temperatures. The increase in SVFS suggests an increase in ferroelectrostriction, consequently resulting in ZTE in the material. Furthermore, the presence of ZTE in BKST10 ceramics is attributed to the relaxor behavior of the material having distinct atomic ordering at various length scales, which will be discussed in the following sections.

D. Raman analysis of BKST10 ceramics

Owing to the relaxor behavior of BKST10 ceramics, the presence of PNRs is obvious. SXR, Raman scattering, and the pair distribution function are the unique techniques used to analyze the symmetry of the materials at different length scales [53]. Temperature-dependent Raman spectra were obtained to analyze the symmetry of BKST10 ceramics at intermediate ranges. Figure 3 depicts the evolution of Raman spectra at 77, 300, and 527 K. The long-range structure of BKST10 ceramics is cubic (space group: $Pm\bar{3}m$) with five triply degenerate phonon modes [56]. Among these, there is one triply degenerate acoustic phonon mode (T_{1u}), and the remaining four are optical phonon modes, which comprise three

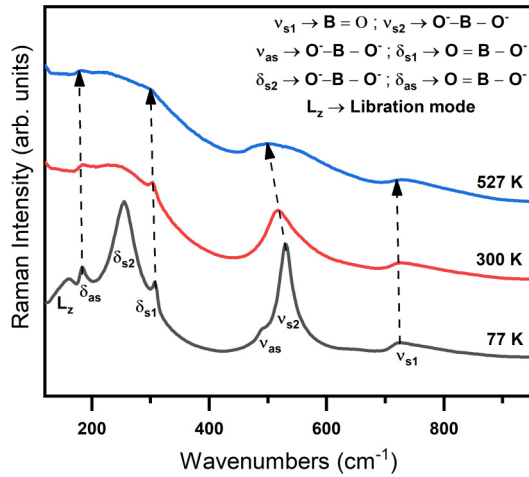


FIG. 3. The Raman spectra of BKST10 ceramics at 77, 300, and 527 K. Descriptions of various modes are given in the top right [54,55] and also in Table VII of the Supplemental Material [43].

polar T_{1u} modes and one nonpolar T_{2u} mode, i.e., $T_{2u} + 3T_{1u}$ [56]. All these phonon modes are Raman inactive, yet we observe Raman peaks in the spectra, which suggests the presence of local distortions (or PNRs) [56]. The observed Raman spectra of BKST10 ceramics feature seven bands (given in Table VII of the Supplemental Material [43]) similar to the rhombohedral phase of BaTiO_3 [54,55]. Among these seven bands, six correspond to the internal vibrations of the BO_3^{2-} anion, while the seventh band (or lowest-frequency band) corresponds to libration mode of BO_6 octahedra [54,57]. The

presence of all these bands in the Raman spectra of BKST10 confirms the rhombohedral symmetry. The six modes corresponding to internal vibrations of BO_3^{2-} are divided into two categories, viz., stretching modes or high-frequency modes (denoted by ν) and bending modes or low-frequency modes (denoted by δ). Both of the modes can be symmetric or asymmetric, represented by a subscript s or as, respectively [54,55]. The presence of $\text{B}=\text{O}$ stretching vibrations (ν_{s1} peak) around 727 cm^{-1} is clear evidence of the polar distortions in BO_6 octahedra [54]. This peak remains present at all three studied temperatures, confirming the existence of polar distortions up to the highest temperature [54,58,59]. Further, the symmetry of BKST10 ceramics at different length scales is analyzed and confirmed using temperature-dependent PDF data, which will be discussed in the next section.

E. PDF analysis of BKST10 ceramics

The symmetry of BKST10 ceramics at various length scales, viz., short and intermediate ranges, can be confirmed using PDF analysis and refinements. We determined the symmetry of BKST10 ceramics at various length scales and three different temperatures, viz., 100, 300, and 500 K. Figure 4 depicts the PDF fits of BKST10 ceramics at 100 K at different length scales for rhombohedral (orange line) and monoclinic (green line) symmetries. Owing to the rhombohedral symmetry concluded from Raman spectra, the $R3m [a_+^0 a_+^0 a_+^0]$ space group was used to refine the PDF data for the range $1.7 \leq r \leq 10 \text{ \AA}$. Various misfits were observed at different bond lengths, as indicated by the black arrows in Fig. 4(a). Thereafter, PDF data were fitted using monoclinic symmetry (space group: $Pm [a_+^0 b_+^0 c_+^0]$) at short ranges ($1.7 \leq r \leq 10 \text{ \AA}$).

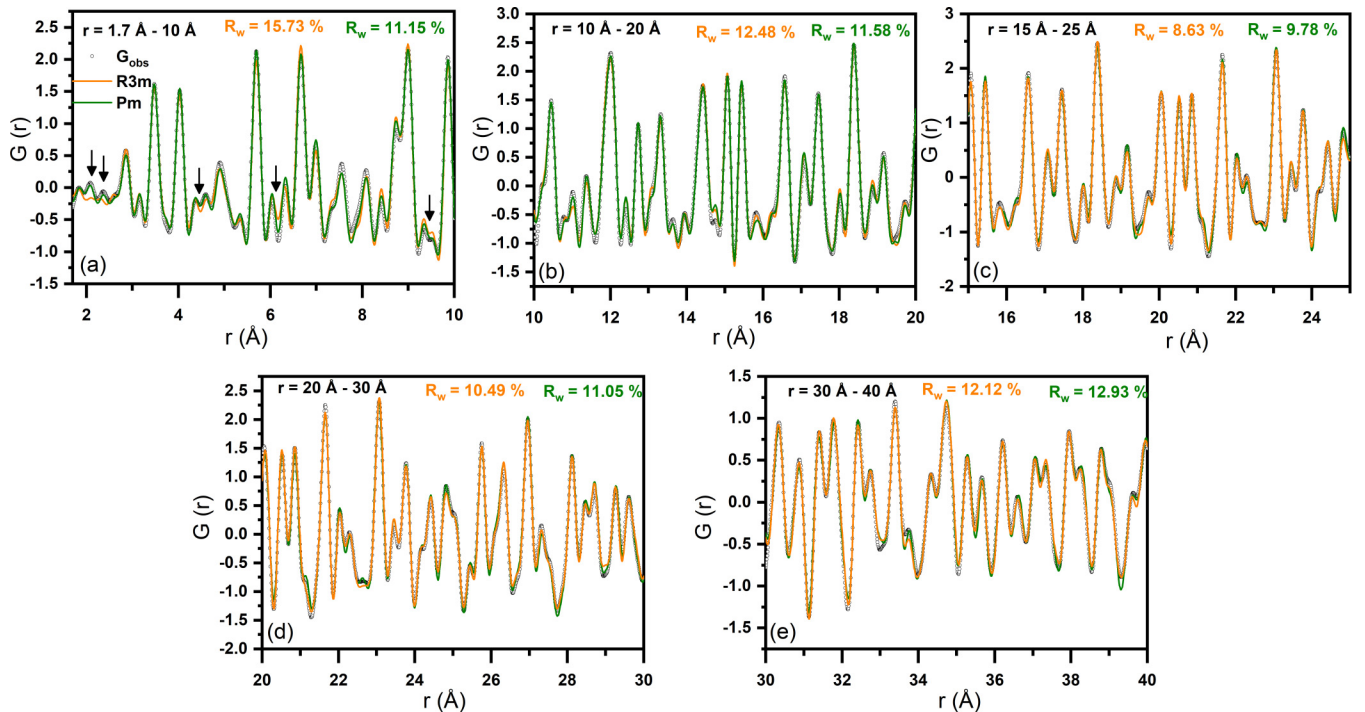


FIG. 4. The fitting of PDF profiles at various length scales, viz., (a) 1.7–10 Å, (b) 10–20 Å, (c) 15–25 Å, (d) 20–30 Å, and (e) 30–40 Å, using the Pm and $R3m$ space groups, where black open circles denote observed PDF data and orange and green lines correspond to $R3m$ and Pm fits, respectively. The arrows represent the misfit observed by the $R3m$ space group at $r \leq 10 \text{ \AA}$.

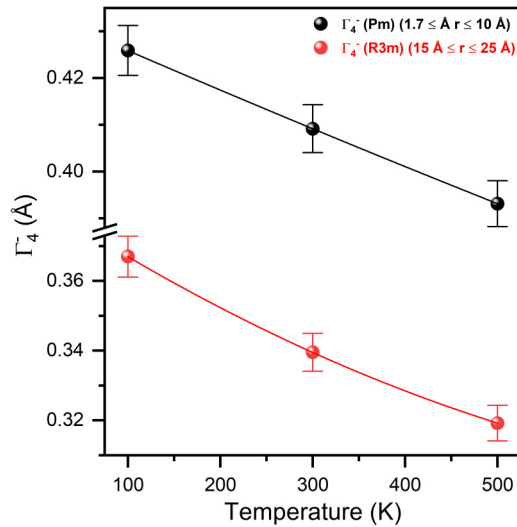


FIG. 5. Temperature-dependent evolution of the amplitude of the ferroelectric phonon mode (Γ_4^-) for the Pm ($1.7 \leq r \leq 10 \text{ \AA}$) and $R3m$ ($15 \leq r \leq 25 \text{ \AA}$) phases.

Here, it is important to note that this monoclinic phase is reported for KNN50 at both long and short ranges stable for wide temperature ranges ($100 \leq T \leq 471 \text{ K}$) [25,33]. This is reminiscent of an earlier report on NaNbO_3 [60]. The PDF fit significantly improves with the Pm space group and gives a lower R_w value for $1.7 \leq r \leq 10 \text{ \AA}$ in comparison to the $R3m$ space group [see Fig. 4(a)], confirming monoclinic (Pm) symmetry at short ranges ($r \leq 10 \text{ \AA}$).

Moreover, at higher interatomic distances i.e., for $r > 10 \text{ \AA}$ (intermediate ranges), the PDF data were fit using the Pm and $R3m$ space groups. It is clearly observed that at intermediate ranges ($r > 10 \text{ \AA}$), the $R3m$ phase fits the PDF data better than the Pm phase, with lower R_w values obtained for the $R3m$ phase at different length scales, viz., $15 \leq r \leq 25 \text{ \AA}$, $20 \leq r \leq 30 \text{ \AA}$, and $30 \leq r \leq 40 \text{ \AA}$ [see Figs. 4(c)–4(e)]. This analysis of PDF fits across various length scales at intermediate ranges confirms the gradual transformation from the Pm to $R3m$ phase at higher length scales, i.e., intermediate ranges. Now, as discussed in the previous section, a rhombohedral symmetry was confirmed at intermediate ranges at all temperatures (77, 300, and 527 K) by Raman scattering. This is further validated via PDF refinements at intermediate ranges, where a rhombohedral phase ($R3m$) gives a better fit relative to the Pm phase observed at short ranges ($r \leq 10 \text{ \AA}$). Hence, PDF analysis at a higher length scale (intermediate ranges) conforms well with the observed Raman spectra.

Furthermore, the PDF refinements were also done for 300 and 500 K at short and intermediate ranges using monoclinic and rhombohedral phases, respectively. The refinements at short ranges ($1.7 \leq r \leq 10 \text{ \AA}$) with monoclinic (Pm) and rhombohedral ($R3m$) space groups at 100, 300, and 500 K are shown in Fig. 5 of the Supplemental Material [43]. The monoclinic symmetry provides better fits (with lower R_w values) for $r \leq 10$ at all the temperatures (see Fig. 5 of the Supplemental Material [43]), confirming the monoclinic phase (Pm) at short ranges for a wide temperature range. Moreover, the rhombohedral phase was confirmed at intermediate ranges using

Raman scattering (see Fig. 3) and PDF data (see Fig. 6 of the Supplemental Material [43]) for a wide temperature range ($100 \leq T \leq 500 \text{ K}$). Further, the structural parameters obtained after PDF refinements at short and intermediate ranges (see Tables IV–VI of the Supplemental Material [43]) are used for symmetry mode analysis in the next section.

F. Frozen phonon mode approach

Static atomic displacements are considered to be responsible for distortions within the unit cell [22,61]. In order to quantify these distortions, the frozen phonon mode approach is considered. The freezing of the phonon mode(s) associated with the cubic Brillouin zone along certain dimensions with equal/unequal magnitudes leads to the stabilization of a low-symmetry phase. The phonon mode responsible for symmetry breaking is referred to as primary, while other phonon modes are referred to as secondary [22,61,62]. A cubic phase ($Pm\bar{3}m$ space group) with lattice parameter $a = 4.00934 \text{ \AA}$ with A -site, B -site, and oxygen atoms fixed at the 1b (0.5,0.5,0.5), 1a (0,0,0), and 3d (0.5,0,0) Wyckoff positions, respectively, is used as the high-symmetry phase. The high-symmetry phase is related to the low-symmetry phase via a group-subgroup relation as follows [20,62,63]:

$$r(\mu, i) = r_0(\mu, i) + u(\mu, i), \quad (6)$$

where $r(\mu, i)$ corresponds to the position of the μ ($= 1, 2, 3, 4, \dots$) atom of the low-symmetry space group, $r_0(\mu, i)$ corresponds to atomic positions of high symmetry, and $u(\mu, i)$ are the static displacements associated with the low-symmetry phase.

Now, in order to quantify the ferroelectric distortions present in the structure at short and intermediate ranges, the amplitudes of symmetry-adapted distortions were calculated using ISODISTORT [41,42]. As discussed earlier, a monoclinic phase (Pm) and a rhombohedral phase ($R3m$) are observed for short and intermediate ranges, respectively. The monoclinic and rhombohedral phases result from the freezing of the triply degenerate ferroelectric phonon mode (Γ_4^-), with OPDs of $(a, 0, b)$ and (a, a, a) , respectively.

Figure 5 depicts the variation of the amplitude of the ferroelectric phonon mode (Γ_4^-) as a function of temperature for short ($1.7 \leq r \leq 10 \text{ \AA}$) and intermediate ($15 \leq r \leq 25 \text{ \AA}$) ranges. The amplitude of the FE phonon mode quantifies the ferroelectric distortions present in PNRs. Moreover, the amplitude of FE phonon mode increases with decreasing temperature (see Fig. 5). This increase in the amplitude of the FE phonon mode can be linked to an increase in the ferroelectric polarization of PNRs. Therefore, enhanced ferroelectric polarization (amplitude of Γ_4^-) at low temperatures can be attributed to thermally induced ferroelectrostriction (volume gain), which can be considered the origin of the zero thermal expansion in the material.

IV. CONCLUSION

In conclusion, distinct atomic nonpolar/polar ordering was observed at various length scales in a ferroelectric relaxor, viz., 0.90(BST10)-0.10(KNN50) (BKST10), determined and quantified by analyzing temperature-dependent real (PDF)

and reciprocal (SXR) space data in conjunction with symmetry mode analysis. Successive ferroelectric phases, viz., monoclinic (Pm) and rhombohedral ($R3m$), were identified at short and intermediate ranges via integrated analysis of temperature-dependent Raman scattering and PDF data. In contrast, a centrosymmetric nonpolar cubic phase ($Pm\bar{3}m$) was confirmed at long ranges using temperature-dependent SXR. The ferroelectric (or polar) distortions observed at short and intermediate ranges were quantified in terms of the amplitude of the ferroelectric phonon mode Γ_4^- . The amplitude of the Γ_4^- phonon mode increases with the decrease in temperature, suggesting an increase in ferroelectric polarization with decreasing temperature. This increase in ferroelectric polarization at short/intermediate ranges, along with an increase in intra-/interpolare cluster interactions, was attributed to the volume gain (ferroelectrostriction) in the

material at low temperatures. Thus, ferroelectrostriction results in ZTE with the linear coefficient of thermal expansion ranging from 0.623 to $10.109 \times 10^{-6} \text{ K}^{-1}$ (100–500 K).

ACKNOWLEDGMENTS

S.T. acknowledges financial assistance from the Defence Research and Development Organisation (Grant No. ERIP/ER/202210003/M/01/1812) and DST-SERB, Government of India (Grant No. CRG/2021/006000). This research used the 28-ID-2 XPD beamline of the National Synchrotron Light Source II, a U.S. Department of Energy (DOE) Office of Science User Facility operated for the DOE Office of Science by Brookhaven National Laboratory under Contract No. DE-SC0012704.

- [1] A. Bokov and Z.-G. Ye, Recent progress in relaxor ferroelectrics with perovskite structure, *J. Mater. Sci.* **41**, 31 (2006).
- [2] A. A. Bokov and Z.-G. Ye, Dielectric relaxation in relaxor ferroelectrics, *J. Adv. Dielectr.* **02**, 1241010 (2012).
- [3] G. Smolenskii, V. Isupov, A. I. Agranovskaya, and S. N. Popov, Ferroelectrics with diffuse phase transitions, *Sov. Phys. Solid State* **2**, 2584 (1961).
- [4] F. Chu, N. Setter, and A. Tagantsev, The spontaneous relaxor-ferroelectric transition of $\text{Pb}(\text{Sc}_{0.5}\text{Ta}_{0.5})\text{O}_3$, *J. Appl. Phys.* **74**, 5129 (1993).
- [5] G. A. Samara, The relaxational properties of compositionally disordered ABO_3 perovskites, *J. Phys.: Condens. Matter* **15**, R367 (2003).
- [6] B. Dkhil, P. Gemeiner, A. Al-Barakaty, L. Bellaiche, E. Dul'kin, E. Mojaev, and M. Roth, Intermediate temperature scale T^* in lead-based relaxor systems, *Phys. Rev. B* **80**, 064103 (2009).
- [7] C. W. Ahn, C.-H. Hong, B.-Y. Choi, H.-P. Kim, H.-S. Han, Y. Hwang, W. Jo, K. Wang, J.-F. Li, J.-S. Lee *et al.*, A brief review on relaxor ferroelectrics and selected issues in lead-free relaxors, *J. Korean Phys. Soc.* **68**, 1481 (2016).
- [8] D. N. Dubey, G. Singh, and S. Tripathi, Relaxor ferroelectricity driven by 'A' and 'B' site off-centered displacements in cubic phase with $Pm\bar{3}m$ space group, *J. Phys. D* **54**, 365304 (2021).
- [9] J. Forrester, E. Kisi, K. Knight, and C. Howard, Rhombohedral to cubic phase transition in the relaxor ferroelectric PZN, *J. Phys.: Condens. Matter* **18**, L233 (2006).
- [10] S. P. Singh, D. Pandey, S. Yoon, S. Baik, and N. Shin, Evidence for monoclinic crystal structure and negative thermal expansion below magnetic transition temperature in $\text{Pb}(\text{Fe}_{1/2}\text{Nb}_{1/2})\text{O}_3$, *Appl. Phys. Lett.* **90**, 242915 (2007).
- [11] T. Maiti, R. Guo, and A. Bhalla, Structure-property phase diagram of $\text{BaZr}_x\text{Ti}_{1-x}\text{O}_3$ system, *J. Am. Ceram. Soc.* **91**, 1769 (2008).
- [12] J. Zhao, A. Glazounov, Q. Zhang, and B. Toby, Neutron diffraction study of electrostrictive coefficients of prototype cubic phase of relaxor ferroelectric $\text{PbMg}_{1/3}\text{Nb}_{2/3}\text{O}_3$, *Appl. Phys. Lett.* **72**, 1048 (1998).
- [13] J. Chen, L. Hu, J. Deng, and X. Xing, Negative thermal expansion in functional materials: Controllable thermal expansion by chemical modifications, *Chem. Soc. Rev.* **44**, 3522 (2015).
- [14] Z. Pan, J. Chen, X. Jiang, L. Hu, R. Yu, H. Yamamoto, T. Ogata, Y. Hattori, F. Guo, X. Fan *et al.*, Colossal volume contraction in strong polar perovskites of $\text{Pb}(\text{Ti},\text{V})\text{O}_3$, *J. Am. Chem. Soc.* **139**, 14865 (2017).
- [15] T. Yang, Y. Wang, L. Fan, N. Wang, K. Lin, J. Chen, and X. Xing, Strong covalent bonding for enhanced negative thermal expansion in $(1-x)\text{PbTiO}_3-x\text{BiGaO}_3$, *J. Phys. Chem. C* **124**, 20445 (2020).
- [16] J. Chen, F. Wang, Q. Huang, L. Hu, X. Song, J. Deng, R. Yu, and X. Xing, Effectively control negative thermal expansion of single-phase ferroelectrics of PbTiO_3 -(Bi, La) FeO_3 over a giant range, *Sci. Rep.* **3**, 2458 (2013).
- [17] H. Yamamoto, T. Imai, Y. Sakai, and M. Azuma, Colossal negative thermal expansion in electron-doped PbVO_3 perovskites, *Angew. Chem., Int. Ed.* **57**, 8170 (2018).
- [18] Z. Pan, X. Jiang, T. Nishikubo, Y. Sakai, H. Ishizaki, K. Oka, Z. Lin, and M. Azuma, Pronounced negative thermal expansion in lead-free BiCoO_3 -based ferroelectrics triggered by the stabilized perovskite structure, *Chem. Mater.* **31**, 6187 (2019).
- [19] A. Tripathi, A. Pandey, J. A. Alonso, R. Erasmus, M. T. Fernandez-Diaz, and S. Tripathi, Origin of zero thermal expansion in an average cubic structure in Pb-free relaxor ferroelectrics, *Appl. Phys. Lett.* **125**, 102901 (2024).
- [20] J. Perez-Mato, D. Orobengoa, and M. Aroyo, Mode crystallography of distorted structures, *Acta Crystallogr., Sect. A* **66**, 558 (2010).
- [21] B. Orayech, A. Faik, G. López, O. Fabelo, and J. Igartua, Mode-crystallography analysis of the crystal structures and the low- and high-temperature phase transitions in $\text{Na}_{0.5}\text{K}_{0.5}\text{NbO}_3$, *J. Appl. Crystallogr.* **48**, 318 (2015).
- [22] A. Tripathi, D. N. Dubey, H. Kumar, and S. Tripathi, Stabilizing ferroelectricity in alkaline-earth-metal-based perovskites (ABO_3) via A -($\text{Ca}^{2+} + \text{Sr}^{2+} + \text{Ba}^{2+}$) and B -site (Ti^{4+}) cationic radius ratio (R_A/R_B), *J. Appl. Crystallogr.* **55**, 1446 (2022).
- [23] V. Buscaglia, S. Tripathi, V. Petkov, M. Dapiaggi, M. Deluca, A. Gajović, and Y. Ren, Average and local atomic-scale structure in $\text{BaZr}_x\text{Ti}_{1-x}\text{O}_3$ ($x = 0.10, 0.20, 0.40$) ceramics by high-energy

- x-ray diffraction and Raman spectroscopy, *J. Phys.: Condens. Matter* **26**, 065901 (2014).
- [24] V. Shvartsman, J. Dec, Z. Xu, J. Banys, P. Keburis, and W. Kleemann, Crossover from ferroelectric to relaxor behavior in $\text{BaTi}_{1-x}\text{Sn}_x\text{O}_3$ solid solutions, *Phase Transitions* **81**, 1013 (2008).
- [25] J. Kong, J. Liu, F. Marlton, M. R. V. Jørgensen, and A. Pramanick, Local structural mechanism for phase transition and ferroelectric polarization in the mixed oxide $\text{K}_{0.5}\text{Na}_{0.5}\text{NbO}_3$, *Phys. Rev. B* **103**, 184104 (2021).
- [26] H. Du, W. Zhou, F. Luo, D. Zhu, S. Qu, and Z. Pei, Phase structure, dielectric properties, and relaxor behavior of $(\text{K}_{0.5}\text{Na}_{0.5})\text{NbO}_3$ - $(\text{Ba}_{0.5}\text{Sr}_{0.5})\text{TiO}_3$ lead-free solid solution for high temperature applications, *J. Appl. Phys.* **105**, 124104 (2009).
- [27] S. Sahoo, D. K. Pradhan, S. Kumari, K. S. Samantaray, C. Singh, A. Mishra, M. M. Rahaman, B. Behera, A. Kumar, R. Thomas *et al.*, Compositional induced structural phase transitions in $(1-x)(\text{K}_{0.5}\text{Na}_{0.5})\text{NbO}_3$ - $x(\text{Ba}_{0.5}\text{Sr}_{0.5})\text{TiO}_3$ ferroelectric solid solutions, *Sci. Rep.* **13**, 19096 (2023).
- [28] Y. Yang, Y. Ji, M. Fang, Z. Zhou, L. Zhang, and X. Ren, Morphotropic relaxor boundary in a relaxor system showing enhancement of electrostrain and dielectric permittivity, *Phys. Rev. Lett.* **123**, 137601 (2019).
- [29] B. Jaffe, W. R. Cook, and H. Jaffe, *Piezoelectric Ceramics* (Academic, London, 1971).
- [30] E. Cross, Lead-free at last, *Nature (London)* **432**, 24 (2004).
- [31] G. Shirane, H. Danner, A. Pavlovic, and R. Pepinsky, Phase transitions in ferroelectric KNbO_3 , *Phys. Rev.* **93**, 672 (1954).
- [32] W. Ge, J. Li, D. Viehland, Y. Chang, and G. L. Messing, Electric-field-dependent phase volume fractions and enhanced piezoelectricity near the polymorphic phase boundary of $(\text{K}_{0.5}\text{Na}_{0.5})_{(1-x)}\text{Li}_x\text{NbO}_3$ textured ceramics, *Phys. Rev. B* **83**, 224110 (2011).
- [33] S. Gupta, V. Petkov, and S. Priya, Local atomic structure of $\text{K}_x\text{Na}_{(1-x)}\text{NbO}_3$ by total x-ray diffraction, *Appl. Phys. Lett.* **105** (2014).
- [34] M. Kumar, A. Garg, R. Kumar, and M. Bhatnagar, Structural, dielectric and ferroelectric study of $\text{Ba}_{0.9}\text{Sr}_{0.1}\text{Zr}_x\text{Ti}_{1-x}\text{O}_3$ ceramics prepared by the sol-gel method, *Physica B (Amsterdam, Neth.)* **403**, 1819 (2008).
- [35] A. Ianculescu, I. Pintilie, C. Vasilescu, M. Botea, A. Iuga, A. Melinescu, N. Drăgan, and L. Pintilie, Intrinsic pyroelectric properties of thick, coarse grained $\text{Ba}_{1-x}\text{Sr}_x\text{TiO}_3$ ceramics, *Ceram. Int.* **42**, 10338 (2016).
- [36] W. Li, Z. Xu, R. Chu, P. Fu, and J. Hao, Sol-gel synthesis and characterization of $\text{Ba}_{(1-x)}\text{Sr}_x\text{TiO}_3$ ceramics, *J. Alloys Compd.* **499**, 255 (2010).
- [37] S. Gel, Effect of strontium on the structural and piezoelectric properties of the sol gel processed barium titanate, *J. Mater. Environ. Sci.* **8**, 4945 (2017).
- [38] E. K. Al-Shakarchi and N. B. Mahmood, Three techniques used to produce BaTiO_3 fine powder, *J. Mod. Phys.* **2**, 1420 (2011).
- [39] V. Petkov, Pair distribution functions analysis, *Charact. Mater.* **1361**, 1 (2012).
- [40] X. Wang, S. Tan, X.-Q. Yang, and E. Hu, Pair distribution function analysis: Fundamentals and application to battery materials, *Chin. Phys. B* **29**, 028802 (2020).
- [41] H. T. Stokes, S. V. Orden, and B. J. Campbell, Isosubgroup: An internet tool for generating isotropy subgroups of crystallographic space groups, *J. Appl. Crystallogr.* **49**, 1849 (2016).
- [42] B. J. Campbell, H. T. Stokes, D. E. Tanner, and D. M. Hatch, Isodisplace: A web-based tool for exploring structural distortions, *J. Appl. Crystallogr.* **39**, 607 (2006).
- [43] See Supplemental Material at <http://link.aps.org/supplemental/10.1103/PhysRevB.111.024104> for the XRD analysis of BKST_x ceramics, microstructure analysis of BKST_x ceramics, the Debye-Grüniesen approximation, a description of Raman modes, PDF measurements, and temperature-dependent PDF analysis, which also contains Refs. [38,50–52].
- [44] D. Garcia, R. Guo, and A. Bhalla, Growth and properties of $\text{Ba}_{0.9}\text{Sr}_{0.1}\text{TiO}_3$ single crystal fibers, *Mater. Lett.* **42**, 136 (2000).
- [45] F. Jona and G. Shirane, *Ferroelectric Crystals* (Macmillan, 1962).
- [46] C. J. Stringer, T. R. Shrout, and C. A. Randall, High-temperature perovskite relaxor ferroelectrics: A comparative study, *J. Appl. Phys.* **101**, 054107 (2007).
- [47] L. K. Pradhan and M. Kar, Relaxor ferroelectric oxides: Concept to applications, in *Multifunctional Ferroelectric Materials*, edited by D. R. Sahu (IntechOpen, Rijeka, Croatia, 2021), Chap. 4.
- [48] S. K. Upadhyay, V. R. Reddy, and N. Lakshmi, Study of $(1-x)\text{BaTiO}_3$ - $x\text{Ni}_{0.5}\text{Zn}_{0.5}\text{Fe}_2\text{O}_4$ ($x = 5, 10$ and 15%) magneto-electric ceramic composites, *J. Asian Ceram. Soc.* **1**, 346 (2013).
- [49] D. B. Migas, V. A. Turchenko, A. Rutkauskas, S. V. Trukhanov, T. I. Zubar, D. I. Tishkevich, A. V. Trukhanov, and N. V. Skorodumova, Temperature induced structural and polarization features in $\text{BaFe}_{12}\text{O}_{19}$, *J. Mater. Chem. C* **11**, 12406 (2023).
- [50] J. Rodríguez-Carvajal, An introduction to the program, Laboratoire Léon Brillouin (2001).
- [51] F. Sayetat, P. Fertey, and M. Kessler, An easy method for the determination of Debye temperature from thermal expansion analyses, *J. Appl. Crystallogr.* **31**, 121 (1998).
- [52] T. Kiyama, K. Yoshimura, K. Kosuge, Y. Ikeda, and Y. Bando, Invar effect of SrRuO_3 : Itinerant electron magnetism of Ru 4d electrons, *Phys. Rev. B* **54**, R756 (1996).
- [53] B. Maier, B. Mihailova, C. Paulmann, J. Ihringer, M. Gospodinov, R. Stosch, B. Güttler, and U. Bismayer, Effect of local elastic strain on the structure of Pb-based relaxors: A comparative study of pure and Ba- and Bi-doped $\text{PbSc}_{0.5}\text{Nb}_{0.5}\text{O}_3$, *Phys. Rev. B* **79**, 224108 (2009).
- [54] T. Sidorov, Structure of BaTiO_3 phases is studied by comparing neutron diffraction and Raman spectroscopy data, *Russ. J. Inorg. Chem.* **56**, 1957 (2011).
- [55] Y. I. Yuzuyuk, Raman scattering spectra of ceramics, films, and superlattices of ferroelectric perovskites: A review, *Phys. Solid State* **54**, 1026 (2012).
- [56] I. Margaritescu, P. D. B. Mihaylova, and K. Datta, Local structure and dynamics of the ferroelectric, Ph.D. Thesis, University of Hamburg, Germany, 2016.
- [57] M. Jauhari, S. Mishra, R. Mittal, and S. Chaplot, Probing of structural phase transitions in barium titanate modified sodium niobate using raman scattering, *J. Raman Spectrosc.* **50**, 1177 (2019).
- [58] L. Veselinović, M. Mitrić, L. Mančić, M. Vukomanović, B. Hadžić, S. Marković, and D. Uskoković, The effect of Sn for Ti substitution on the average and local crystal structure of $\text{BaTi}_{1-x}\text{Sn}_x\text{O}_3$ ($0 \leq x \leq 0.20$), *J. Appl. Crystallogr.* **47**, 999 (2014).

- [59] I. Margaritescu, K. Datta, J. Chen, and B. Mihailova, Distinct temperature behavior of the local structure of $(1-x)\text{PbTiO}_3-x\text{BiNi}_{0.5}\text{Ti}_{0.5}\text{O}_3$ at the morphotropic phase boundary, *J. Raman Spectrosc.* **51**, 1200 (2020).
- [60] L. Jiang, D. C. Mitchell, W. Dmowski, and T. Egami, Local structure of NaNbO_3 : A neutron scattering study, *Phys. Rev. B* **88**, 014105 (2013).
- [61] W. Cochran, Crystal stability and the theory of ferroelectricity, *Phys. Rev. Lett.* **3**, 412 (1959).
- [62] D. Orobengoa, C. Capillas, M. I. Aroyo, and J. M. Perez-Mato, Amplitudes: Symmetry-mode analysis on the Bilbao Crystallographic server, *J. Appl. Crystallogr.* **42**, 820 (2009).
- [63] H. Kumar, A. Singh, J. L. Martinez, J. A. Alonso, and S. Tripathi, Unexplored signatures of magnetoelastic and isosymmetric metal-insulator phase transition in a rare-earth nickelate via mode crystallography, *Phys. Rev. B* **106**, 214103 (2022).